

1 Changes in global teleconnection patterns under global warming and stratospheric aerosol
2 intervention scenarios

3 **Abolfazl Rezaei^{1,2,*}, Khalil Karami³, Simone Tilmes⁴, & John C. Moore⁵**

4
5 ¹ Department of Earth Sciences, Institute for Advanced Studies in Basic Sciences, Zanjan 45137-
6 66731, Iran. arezaei@iasbs.ac.ir; abolfazlrezaei64@gmail.com.

7 ² Center for Research in Climate Change and Global Warming (CRCC), Institute for Advanced Studies
8 in Basic Sciences (IASBS), Zanjan 45137-66731, Iran.

9 ³ Institut für Meteorologie, Stephanstraße 3, 04103 Leipzig, Germany. khalil.karami@uni-leipzig.de

10 ⁴ National Center for Atmospheric Research, Boulder, CO, USA. tilmes@ucar.edu

11 ⁵ Arctic Centre, University of Lapland, Rovaniemi, 96101, Finland.

12
13 * Corresponding Author: Abolfazl Rezaei, Department of Earth Sciences, Institute for Advanced
14 Studies in Basic Sciences, Zanjan 45137-66731, Iran. arezaei@iasbs.ac.ir;
15 abolfazlrezaei64@gmail.com.

16
17
18 **Abstract**

19 We investigate the potential impact of Stratospheric Aerosol Intervention (SAI) on the
20 spatiotemporal behavior of large-scale climate teleconnection patterns represented by the North
21 Atlantic Oscillation (NAO), Pacific Decadal Oscillation (PDO), El Niño/Southern Oscillation (ENSO)
22 and Atlantic Multidecadal Oscillation (AMO) indices using simulations from the Community Earth
23 System Models (CESM1 and CESM2). The leading Empirical Orthogonal Function of sea surface
24 temperature (SST) anomalies indicates that greenhouse gas (GHG) forcing is accompanied by
25 increases in variance across both the North Atlantic (i.e., AMO) and North Pacific (i.e., PDO) and a
26 decrease over the tropical Pacific (i.e., ENSO); however, SAI effectively reverses these global
27 warming-imposed changes. The projected spatial patterns of SST anomaly related to ENSO show no
28 significant change under either global warming or SAI. In contrast, the spatial anomaly patterns
29 pertaining to AMO (i.e., in the North Atlantic) and PDO (i.e., in the North Pacific) changes under global
30 warming are effectively suppressed by SAI. For AMO, the low contrast between the cold-tongue
31 pattern and its surroundings in the North Atlantic, predicted under global warming, is restored under
32 SAI scenarios to similar patterns as in the historical period. The frequencies of El Niño and La Niña
33 episodes modestly increase with GHG emissions in CESM2, while SAI tends to compensate for them.

34 All climate indices' dominant modes of inter-annual variability are projected to be preserved in both
35 warming and SAI scenarios. However, the dominant decadal variability mode changes in the AMO,
36 NAO, and PDO induced by global warming are not suppressed by SAI.

37

38 **Keywords:** Ocean-atmosphere teleconnection patterns; GLENS; SSP5-8.5; Stratospheric Aerosol
39 Intervention; Global warming

40

41 **500-character non-technical text**

42 Teleconnection patterns are important characteristics of the climate system, well-known examples
43 include the El Niño and La Niña events driven from the tropical Pacific. We examined how
44 spatiotemporal patterns that arise in the Pacific and Atlantic Oceans behave under stratospheric
45 aerosol geoengineering and greenhouse gas (GHG)-induced warming. In general, geoengineering
46 reverses trends, however, the changes in decadal oscillation for the AMO, NAO, and PDO imposed by
47 GHS are not suppressed.

48

49 **1. Introduction**

50 Although the Paris agreement and accompanying international commitments to decrease carbon
51 emissions are an essential step forward, current nationally contributions have only about a 50%
52 chance to restrict global mean temperature increase to 2°C above preindustrial (Meinshausen et al.,
53 2022). Exceeding 2°C will lead to severe consequences and societal disruption worldwide as
54 humanity is critically dependent on ecosystems, food, fresh water, and health systems which face
55 rapidly challenging adaptation pressure above 2°C of global warming (Field and Barros, 2014).

56 In parallel with emissions reductions, solar radiation modification (SRM) has been suggested to limit
57 global temperature increases and consequent climate impacts from anthropogenic greenhouse gas
58 (GHG) emissions. A naturally occurring analog of SRM is the well-known global surface cooling
59 following large volcanic eruptions, albeit over relatively short periods. Simulations have shown that
60 SRM decreasing total solar irradiance by about 2%, would roughly compensate for global warming
61 from a doubling of CO₂ concentrations (Dagon and Schrag, 2016).

62 Oceans act as major drivers of climate variability worldwide (e.g., Shukla, 1998; Cai et al., 2021), and
63 more than 90% of the excess energy balance of the earth arising from GHG emissions ends up heating
64 the ocean (Cheng et al., 2015). Variations in sea surface temperatures (SSTs) and the global climate
65 are linked through ocean-atmosphere energy exchanges that can be helpfully summarized by climate
66 indices that characterize large-scale climate teleconnection patterns. That is recurring and

67 persistent, large-scale anomaly patterns of pressure and circulation across large geographical
68 regions. Some of the most referred to are El Niño/Southern Oscillation (ENSO), Pacific Decadal
69 Oscillation (PDO), Atlantic Multidecadal Oscillation (AMO), and North Atlantic Oscillation (NAO). The
70 dominant inter-annual feature of climate variability on the planet is ENSO, and its state produces
71 widespread climatic and environmental outcomes (Latif and Keenlyside, 2009). The PDO modulates
72 marine ecosystems and global climate on decadal time scales (Mantua et al., 1997), impacts ENSO
73 onset and frequency (Fang et al., 2014), and is useful for short- to long-term climate forecast (An and
74 Wang, 1999). The AMO has broader hemispheric impacts beyond North American and European
75 climates (Enfield et al. 2001), influencing the monsoons across North African, East Asia, and India
76 (Zhang and Delworth 2006). The NAO is among the dominant climate variability modes in the
77 northern hemisphere (Simpkins, 2021).

78 Several studies have explored how climate indices, particularly ENSO, respond to global warming
79 and increasing GHG concentrations. Statistically significant systemic changes have occurred in ENSO
80 dynamics and the evolution of El Niño and La Niña events since the 1960s (Moron et al., 1998;
81 Capotondi and Sardeshmukh, 2017). ENSO may favor more severe events under global warming
82 (Fedorov and Philander, 2001), and Cai et al. (2015) found that ENSO-associated disastrous weather
83 consequences tend to arise more frequently under unabated CO₂ emissions. Cai et al. (2021) found
84 an inter-model consensus on increases in forthcoming ENSO rainfall and temperature fluctuations
85 under increasing GHG concentrations. The PDO, which is essentially the extra-tropical manifestation
86 of ENSO, is simulated with a similar spatial pattern as at present under various future climates but
87 with reduced amplitude and a shorter characteristic time scale (e.g., Zhang and Delworth, 2016). The
88 North Atlantic is a key ocean for investigating global climate changes (Wang and Dong, 2010), and
89 acts as a major carbon dioxide sink (Watson et al., 2009). Atmospheric CO₂ concentrations vary with
90 the phase of the AMO with the warm phase associated with lowered atmospheric CO₂ (Wang and
91 Dong, 2010). The two NAO action points in the Icelandic low and the Azores high have been projected
92 to significantly intensify and shift northeastward by 10-to-20° in latitude and 30-to-40° in longitude
93 in response to global warming (Hu and Wu, 2004).

94 Stratospheric Aerosol Intervention (SAI), is a type of SRM that has been widely simulated by many
95 global climate models (e.g., Kravitz et al., 2013), which is accompanied by changing in global
96 circulations such as the NAO teleconnection pattern (Moore et al., 2014), and is known in various
97 models to partially offset the decline in the Atlantic Meridional Overturning Circulation (AMOC; Xie
98 et al., 2022). Undorf et al. (2018) simulated the North Atlantic SST cooling accompanied by the
99 historical rise of stratospheric sulfate aerosol from North America and Europe dating back to 1850-

100 1975. Gabriel and Robock (2015) is the only study to date that explores the effects of SAI in multiple
101 models on the possible amplitude and frequency changes of El Niño/Southern Oscillation (ENSO).
102 They concluded that changes in ENSO in the SAI simulations were either not present or not large
103 enough to be captured by their approach, given the across-model variability issue. Thus, little is
104 known about possible changes that future global climate change scenarios with artificial cooling may
105 have on ocean-atmosphere climate indices. Recently, a novel set of SRM models have been globally
106 complete with the state-of-the-art climate models: Community Earth System Model versions 1 and
107 2 (CESM1 and CESM2). These models have improved planetary boundary layer turbulence, aerosols,
108 radiation, and cloud microphysics which should enable more reliable for the forthcoming global
109 climate change projections (Mills et al., 2017).

110 We use the Geoengineering Large Ensemble Simulation (GLENS) with 20 members from a single
111 model, the Community Earth System Model 1 (CESM1) with Stratospheric Aerosol Intervention
112 (GLENS-SAI), to explore the possible changes in climate teleconnection patterns under future climate
113 change scenarios. The models use the Representative Concentration Pathway (RCP) 8.5 high GHG
114 emissions forcing state (Riahi et al., 2011) as a baseline and increase stratospheric sulfur injections
115 through the century, to maintain global surface temperatures at 2020 levels. This produces an
116 increasingly large signal-to-noise ratio through the 21st century. In addition, we use recent
117 simulations (SSP5-8.5-SAI) with an updated model version (CESM2). For these simulations, the SSP5-
118 8.5 GHG emissions scenarios were used as the GHG baseline on which SAI was performed. The two
119 different model experiments show some surprising differences in the required sulfur injections and
120 climate outcomes with and without SAI applications (Fasullo et al., 2020, Tilmes et al., 2020). Thus,
121 even models from different generations in the same family can produce sufficiently different climates
122 to explore a range of plausibly real climate impacts. The goal of this study is to identify robust features
123 across the two model versions in the response of climate indices (ENSO, PDO, AMO and NAO) to GHG
124 induced global warming and its compensation by SAI.

125 We employed empirical orthogonal functions and wavelet transforms to decompose time series and
126 study the differences in the climate teleconnection patterns between the SSP5-8.5 and SSP5-8.5-SAI
127 scenarios. Since teleconnection patterns are emergent features of the non-linear, chaotic climate
128 system (Ghil et al., 2002), their underlying physical causes are complex and not necessarily the same
129 in any model as on the real planet. Hence, we assess the potential changes in temporal and spatial
130 characteristics of climate indices of AMO, NAO, ENSO, and PDO under both extreme warming GHG
131 scenarios and with SAI employed to mitigate those warmings while maintaining extreme GHG
132 concentration trajectories.

133 **2. Data and Methods**

134 **2.1. Models and scenarios**

135 We used two SAI models and scenarios: (1) CESM1 for GLENS-SAI and (2) CESM2 for SSP5-8.5-SAI.
136 The GLENS simulations were done by the Community Earth System Model version 1 (CESM1) with
137 the Whole Atmosphere Community Climate Model (WACCM) as the atmospheric system integrated
138 to land, ocean, and sea ice models (Mills et al., 2017). The resolution of atmospheric component is
139 1.25° in longitude and 0.9° in latitude. A 20-member reference simulation for the RCP8.5 scenario
140 (Riahi et al., 2011) over the 2010–2030 period with three ensemble members (001 to 003)
141 continuing up to the end of the 21st century. GLENS-SAI is a 20-member ensemble of stratospheric
142 sulfur dioxide (SO₂) injection simulations, spanning 2020-2099. Each ensemble member was begun
143 in 2010 with small differences in their initial air temperatures, while their ocean, sea-ice, and land
144 temperatures were the same. Even before the start of the SAI injections in 2020, the fully coupled
145 model produced variability between the ensemble members due to its chaotic nature. Here, we use
146 all available members of the RCP8.5 and GLENS-SAI simulations, which extend until the end of the
147 21st century. For the analysis, we used monthly SST and sea-level pressure (PSL) from CESM1 with
148 length of 1980-2009 for the historical period, 2010-2099 for global warming, and 2020-2099 for SAI.
149 We also analyzed output from the NCAR Community Earth System Model version 2- Whole
150 Atmosphere Community Climate Model Version 6 (CESM2(WACCM6)). This model version was used
151 for performing the Coupled Model Intercomparison Project Phase 6 (CMIP6; Eyring et al., 2016)
152 simulations. Like GLENS, this SAI experiment is according to the high GHG emissions scenario, called
153 SSP5-85 in CMIP6, (SSP5-8.5-SAI) and limits mean global temperatures to 1.5°C above 1850–1900
154 conditions, which without SAI, is exceeded around the year 2020 in CESM2(WACCM6) under SSP5-
155 8.5. The experiment used sulfur injection locations at the same four latitudes as in GLENS to
156 accomplish the same three temperature goals (Tilmes et al., 2020). We used the monthly SST and PSL
157 data from all five members (r1 to r5) of the SSP5-8.5 scenario (covering 2015-2100) and the three
158 available ensemble members of SSP5-8.5-SAI that cover the period of 2020-2100. For the analysis,
159 we also applied a one-member historical simulation based on the specific CESM1(WACCM) version
160 used for GLENS between 1980-2009 (denoted as “historical” in the following). All three
161 corresponding members (r1 to r3) from the CESM2(WACCM6) version were used for the historical
162 period. For wavelet analysis modes in Sections 2.3 and 3.2, we used the entire length (1850-2014) of
163 the available historical outputs from CESM2, but for spatial changes patterns in Section 3.1, the data
164 that cover the 1980-2009 historical period were used for consistency with CECM1.

165 The SAI scenarios using both CESM1 and CESM2 inject SO₂ at four predefined points (30°N, 30°S,
166 15°N, and 15°S) at ~5 km above the tropopause using a feedback controller to maintain not just the
167 global mean temperature, but the interhemispheric and equator-to-pole temperature gradients.
168 Fasullo and Richter (2022) explain the inter-model differences in the aerosol mass latitudinal
169 distributions between the SAI experiments using CESM1 and CESM2. CESM2 SAI utilizes the CMIP6
170 SSP5-8.5 experiment as a baseline which has been used by various modeling teams (Tilmes et al.,
171 2020) while CESM1 SAI uses the well-known RCP8.5 scenario. In GLENS-SAI, most of the aerosols
172 were injected at 30°N and 30°S with much smaller injection mass at 15°N and a tiny amount at 15°S
173 while for SSP5-8.5-SAI, the highest concentrations were released at 15°S, modest mass at 15°N and
174 30°S, and a small amount at 30°N. These differences in the SO₂ distributions across the two SAI
175 scenarios for CESM1 and CESM2 produce a range of variability in shortwave radiation and cloud
176 responses to CO₂ concentration increases (Fasullo and Richter, 2022). Additionally, Fasullo and
177 Richter (2022) identified that changes in the spatial salinity and density patterns in the Atlantic
178 Ocean, and in turn, the Atlantic Meridional Overturning Circulation (AMOC), are very different under
179 GLENS-SAI compared to SSP5-8.5-SAI experiment. These differences between SAI simulations
180 represent part of the system variability.

181 The equilibrium climate sensitivity (ECS) of CESM2-WACCM is 4.75 °C and lies in an ECS range of 1.83
182 to 5.67 °C from 41 different CMIP6 GCMs (IPCC AR6, 2021). The absolute mean surface temperature
183 difference between CESM2-WACCM and historical records (0.89 °C) and is also within the range of
184 0.38-1.23 °C from 37 different CMIP6 models (Scafetta, 2021). CESM2 is one of the best nine models
185 for simulating precipitation worldwide when measured by the Hellinger distance between bivariate
186 empirical densities of 34 CMIP6 models and the historical data from Global Precipitation Climatology
187 Centre (GPCC; Abdelmoaty et al., 2021). Additionally, the global-mean values of SST, summer land
188 temperatures, precipitation, and ECS simulated by CESM1 and CESM2 are roughly similar to each
189 other as well as compatible with the historical values over the 1985-2014 period (Danabasoglu et al.,
190 2020; Table S1).

191 Relative to the preindustrial 1851-1850 period, CESM2-WACCM projects global mean surface air
192 temperature rises of ~6.25 °C by the 2071-2100 period under SSP5-8.5 which compares with the
193 range of ~3.3-6.6 °C from 35 ensembles of 12 CMIP6 models (Cook et al., 2020).

194

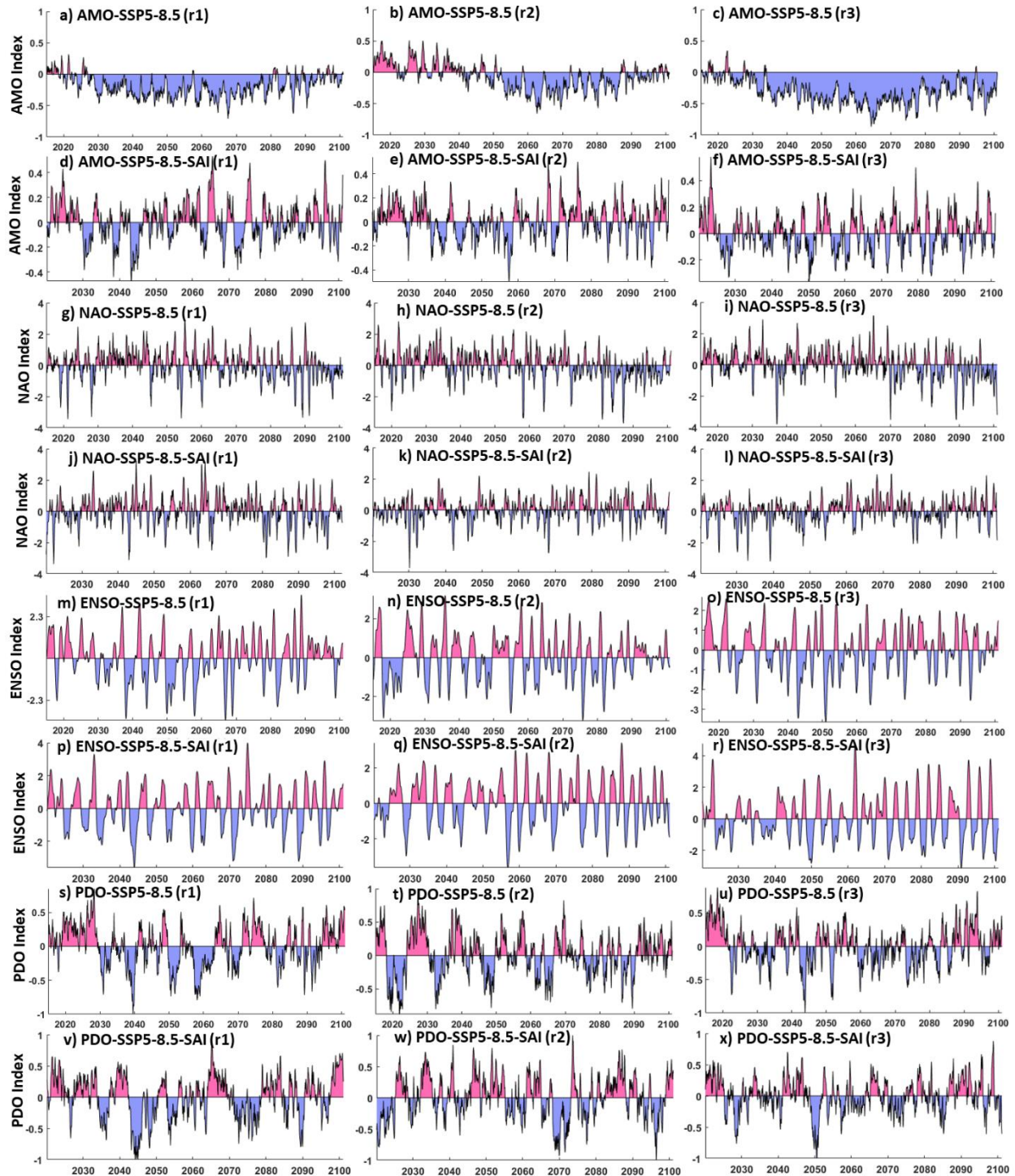
195 **2.2. Climate indices**

196 The AMO was calculated from the area-weighted average of SSTs across the northern Atlantic from
197 0-70° N. The NAO was computed from the PSL time series at two stations: Gibraltar (to the south of

198 Spain; around 36.1°N and 5.3°W) and Reykjavik (in the southwest of Iceland; around 64.1°N and
199 22.0°W). The ENSO index follows the definition proposed by Trenberth (1997). Here, we used SSTs
200 at the Niño 3.4 region (east-central equatorial Pacific between 5°N-5°S, 170°W-120°W) as a proxy
201 for ENSO. After removing the global mean SST anomaly, the leading Empirical Orthogonal Function
202 (EOF) of monthly SST anomalies across the North Pacific (20°-70°N) is termed PDO following Mantua
203 et al. (1997). All these computations were analyzed through the Climate Data Toolbox prepared by
204 Greene et al. (2019). As an example, Fig. 1 compares AMO, NAO, ENSO, and PDO indices obtained
205 from SSP5-8.5 and SSP5-8.5-SAI scenarios.

206 We characterized ENSO by El Niño and La Niña episodes. The ENSO index positive and negative
207 episodes correspond to El Niño and La Niña, respectively. Consistent with Gabriel and Robock (2015),
208 ENSO episodes were identified as departures of at least 0.5 standard deviations from zero in a five-
209 month running averaged ENSO time series. Each episode was characterized by its duration (years),
210 the extreme peak excursion (°C), and the width at half extreme height (years).

211



212

213 **Figure 1.** AMO (panels a-f), NAO (panels g-l), ENSO (i.e., NINO3.4, panels m-r), and PDO (panels s-x)
 214 indices obtained from ensemble members r1(left column), r2 (middle column), and r3 (right
 215 column) of the SSP5-8.5 (odd rows) and SSP5-8.5-SAI (even rows) scenarios.

216

217

218 2.3. Spatiotemporal analyses

219 Analyses in both space and time as well as modes of variability ranging from the inter-annual to
220 decadal changes were used to identify the possible changes in the large-scale climate circulations
221 resulting from global warming and SAI scenarios. EOF analysis is commonly used to extract the
222 climate variability space-time modes (e.g., Chen and Tung, 2018; Joyce, 2002). We applied EOF to
223 extract the first (dominant) modes of de-trended non-seasonal-SST and its corresponding variance
224 across the North Atlantic and North Pacific, which are related to the AMO and PDO respectively. As
225 ENSO is the primary indicator of global climate variability, we used the leading EOF of global SST
226 anomalies in the study of ENSO.

227 The continuous wavelet transform (CWT) is commonly used to capture the primary characteristics
228 of signals (Addison, 2018). For a time series $(x_n, n=1, \dots, N)$ having regular time intervals δt , the
229 CWT is computed as the convolution of x_n with the scaled and normalized wavelet (e.g., here we use
230 the Morlet wavelet which gives reasonably equal weighting and resolution in time and period space;
231 Grinsted et al., 2004):

$$232 \quad W_n^x(s) = \sqrt{\frac{\delta t}{s}} \sum_{n'=1}^N x_{n'} \psi_0 \left[(n' - n) \frac{\delta t}{s} \right] \text{ where } \psi_0(\eta) = \pi^{-1/4} e^{i\omega_0 \eta} e^{-0.5\eta^2} \quad (1)$$

233 where s is the wavelet scale, ψ_0 the Morlet wavelet, ω_0 dimensionless frequency, $[\ast]$ the complex
234 conjugate, and η dimensionless time. The noise spectrum assigned to generate significance testing
235 is a key issue in time series analysis. We concurred with the widely-used red-noise null hypothesis
236 methodology based on 1000 synthetic series with the same mean, standard deviation and first-order
237 autoregressive coefficient as the target time series produced by Monte Carlo approaches to estimate
238 the significance of the CWT (Grinsted et al., 2004). Additionally, for each time series, CWT's global
239 power spectrum was calculated as a function of time. The global power spectrum provides insight
240 into the dominant temporal modes of variability of each climate index within each ensemble member
241 for the reference GHG and SAI scenarios. The wavelet method cone of influence automatically shows
242 where the periods analyzed are being influenced by the end of the time series. Thus, the longest
243 periods can only be reliably assessed for the middle of the time series.

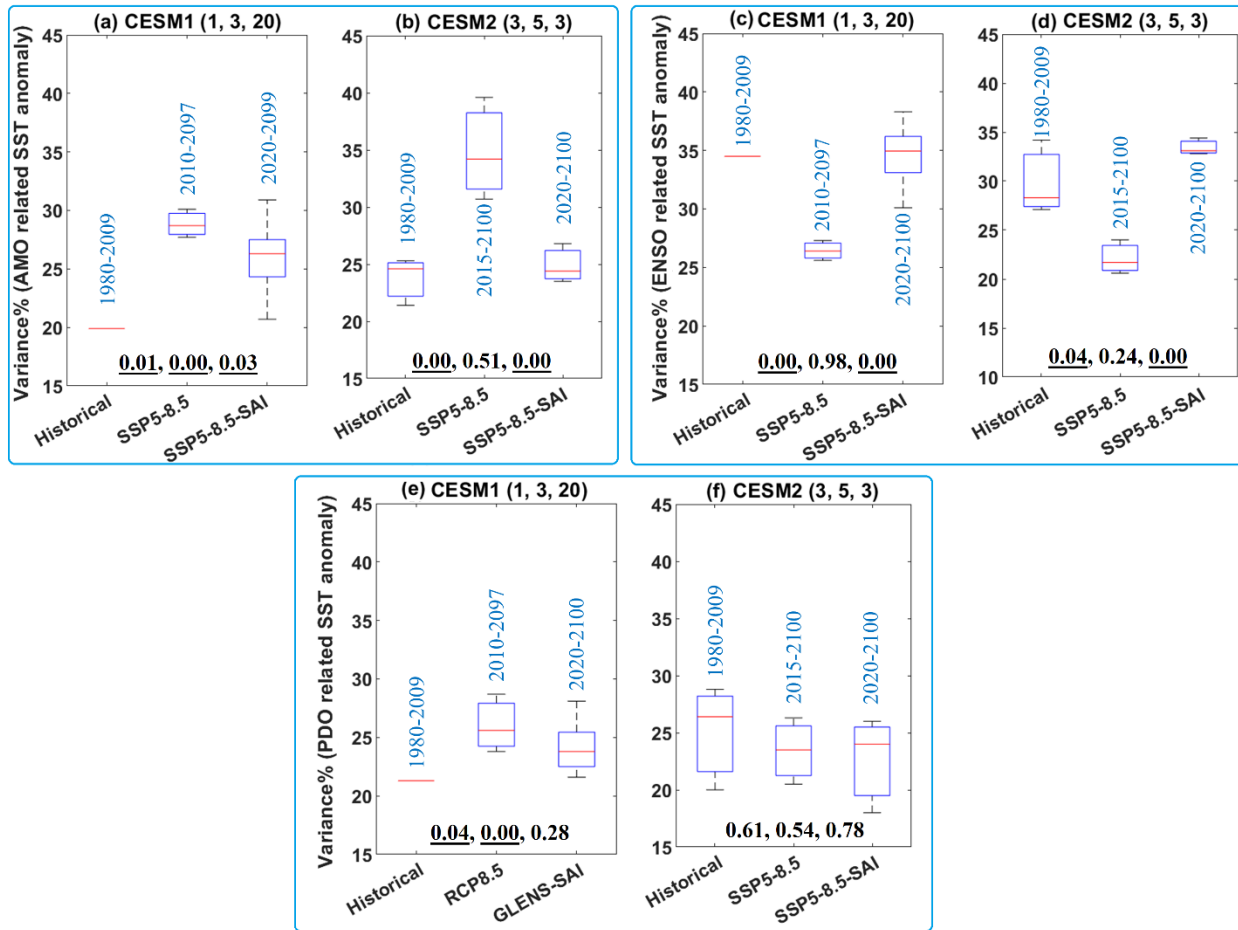
244 The individual ensemble members are treated as independent of each other in calculating the
245 statistics of the ensembles. The CWT was conducted on monthly ENSO time series, and the 12-month
246 moving averaged low-pass filtered signals of AMO, NAO, and PDO. We always use the longest
247 available record length in every ensemble member to gain maximum statistical power to establish
248 significant differences between experiments.

249 **3. Results:**

250 **3.1. Changes in the spatial patterns**

251 Figure 2 reveals the projected changes in the variance of the SST anomalies related to the AMO (i.e.,
252 across the North Atlantic), ENSO (i.e., global scale), and PDO (i.e., across the North Pacific) based on
253 CESM1 and CESM2 results. Figure S1 shows three different plots for the CESM1 as the time period of
254 the 20-member ensemble for RCP8.5 differ: ensembles 001 to 003 (2010-2097) are longer than the
255 other 17 ensemble members (2010-2030). For RCP8.5 and SSP5-85 using CESM1 and CESM2,
256 respectively, the strong GHG forcing and global warming to the end of the 21st century increases the
257 variance of the first EOF SST anomaly in the North Atlantic and North Pacific (representing AMO and
258 PDO), but reduces the variance of the leading EOF in global SST anomaly (related to ENSO). Based on
259 the statistical t-test results, the changes in the means imposed by global warming relative to historical
260 are all significant except one case (Fig. 2f). Differences between SAI and historic in CESM2 values of
261 the leading EOF variance of AMO and ENSO are not significant, showing that the significant changes
262 under GHG forcing are effectively reversed by SAI. In contrast, the changes in PDO variance imposed
263 by global warming using CESM1 relative to historical remain significant under SAI. Using CESM2,
264 there is no significant changes in the PDO variance from historical to global warming, or to SAI.

265

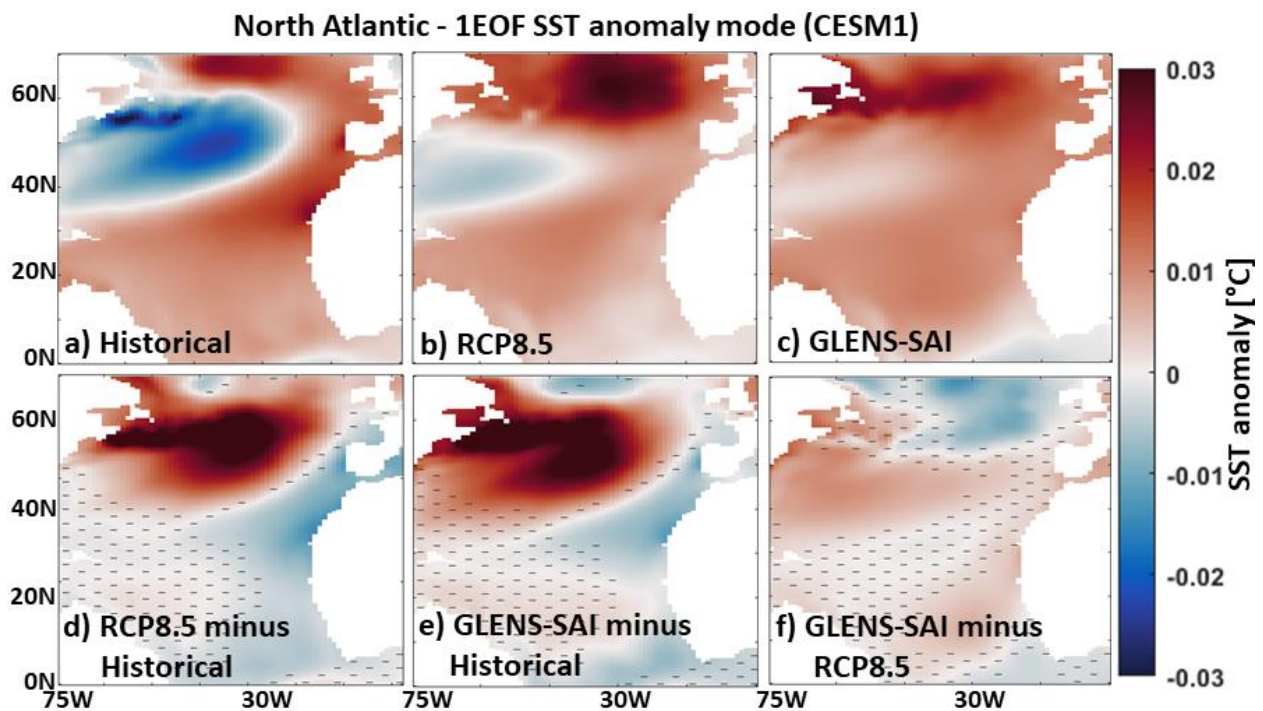


266

267 **Figure 2.** Box and whiskers plot of the variance in the leading EOFs, representing AMO, PDO, and
 268 ENSO, relative to the total variance of the SST fields: AMO across the North Atlantic (top-left panel);
 269 ENSO (top-right panel) global SST; and PDO across the North Pacific (bottom panel). The values in
 270 blue on each column box show the period of the data for historical, GHG (i.e., RCP-8.5 and SSP5-8.5),
 271 and climate intervention (GLENS-SAI and SSP5-8.5-SAI) scenarios. The titles of each subplot refer to
 272 the CESM version and the number of ensembles used in the historical, GHG (RCP8.5 and SSP5-8.5),
 273 and SAI (GLENS-SAI or SSP5-8.5-SAI) scenarios, respectively. The median for each experiment is
 274 denoted by the red line, the upper (75th) and lower (25th) quartiles by the top and bottom of the box
 275 and ensemble limits by the whisker extents. The three values shown at bottom of each sub-plot
 276 refer to the p-values obtained from the statistical t-test between historical and global warming,
 277 historical and SAI, and global warming and SAI, respectively. Values underlined are significant (i.e.,
 278 $p < 0.05$)
 279

280 Figures 3-6 and S2-S3 show the spatial anomalies of the leading EOF mode of the SST in the North
 281 Atlantic, North Pacific, and tropical pacific under both the CESM1 and CESM2. For the historical
 282 period, there is a cold-tongue pattern in the North Pacific broadens from the western to the eastern
 283 parts surrounded by warm water, particularly to the north. GHG related global warming lowers the
 284 contrast between the cold-tongue pattern and its surroundings and increases the water temperature
 285 inside the cold-tongue-pattern, and also leads to a substantial expansion of a warm-pattern in the

286 north. The same patterns (Fig. 4) are also obtained under SSP5-8.5 using CESM2. SAI effectively
 287 shrinks the warm pattern in the northern Atlantic under the RCP8.5 and SSP5-8.5 through a
 288 significant SST decrease, particularly using CESM1 (bottom row in Figs. 3 and 4). The SSP5-8.5-SAI
 289 experiment increases the temperature contrast in the cold-tongue pattern, while the GLENS-SAI does
 290 not. The projected changes in the spatial SST patterns across the North Atlantic, observed under
 291 global warming, are significantly suppressed under SAI (Figs. 3f and 4f). This response of AMO to SAI
 292 is compatible with the observed changes in AMO imposed by anthropogenic and volcanic aerosols
 293 reported by Masson-Delmotte et al. (2021). Anthropogenic and volcanic aerosols are understood to
 294 have impacted the timing and magnitude of the cold (negative) episode in the historical AMO record
 295 between the mid-1960s and mid-1990s and succeeding warming (Masson-Delmotte et al., 2021).
 296 Anthropogenic aerosols have also been suspected as impacting historical SSTs elsewhere,
 297 particularly the decadal ENSO variability (e.g., Sutton and Hodson, 2007; Westervelt et al., 2018).
 298



299
 300 **Figure 3.** The first EOF (1EOF) patterns of SST anomaly across the North Atlantic relate to the AMO
 301 index simulated by CESM1 for the historical data (a) and the mean of the available ensemble
 302 members outputs under the RCP8.5 (b) and GLENS-SAI (c) scenarios. The maps at the bottom row
 303 show RCP8.5 minus historical (d), GLENS-SAI minus historical (e), and GLENS-SAI minus RCP8.5 (f)
 304 where the hatched patterns are not statistically significant ($p > 0.05$), based on p-values from t-test
 305 analysis.

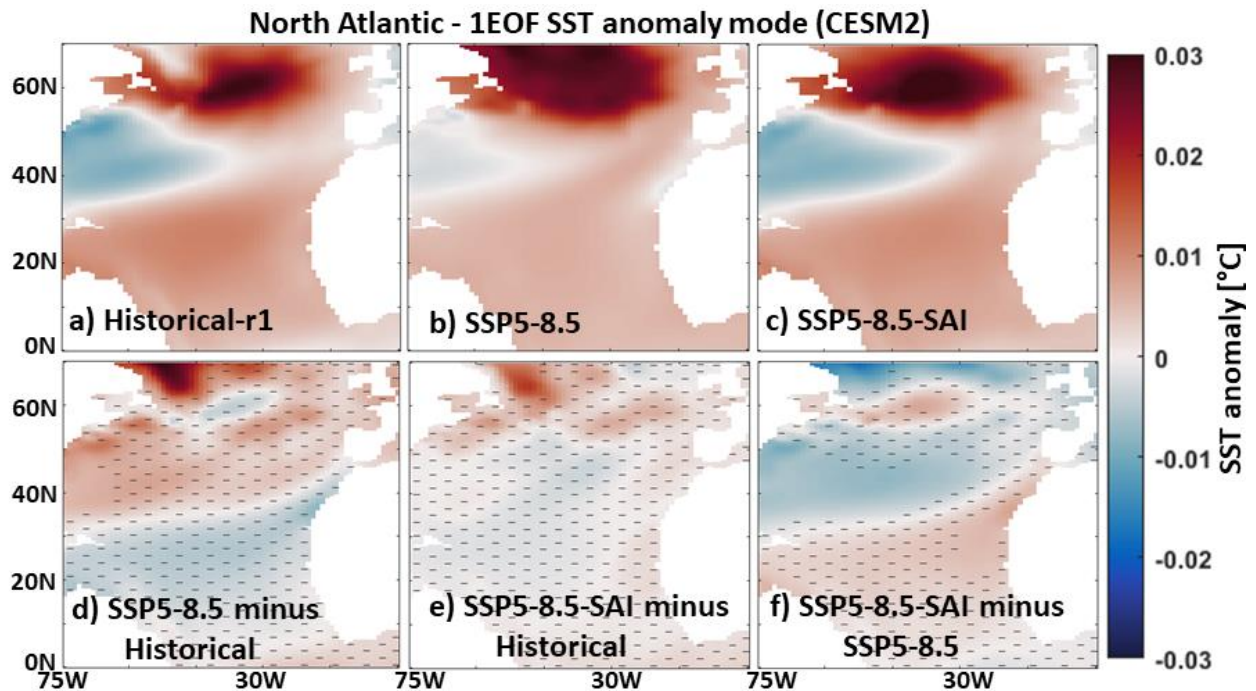


Figure 4. As in Fig. 3, but for CESM2 and SSP5-8.5.

306

307

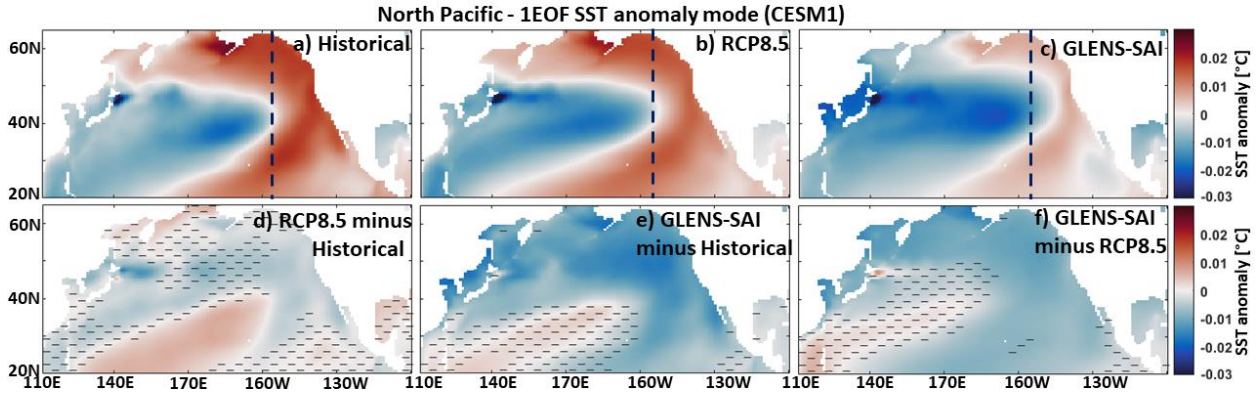
308

309 The leading EOF of monthly global SST anomalies corresponding to the ENSO mode (Figs. S2 and S3),
 310 and is seen as a warm-tongue pattern over the tropical Pacific, that exhibits very similar patterns
 311 under both global warming and SAI scenarios as in the historical period. However, Fig. S4 shows that
 312 the warm-tongue pattern in CESM1 and CESM2 has an excessive westward extension relative to
 313 observations, which is compatible with the findings of Capotondi et al. (2020).

314 While the first EOF SST anomaly across the North Pacific under both global warming and SAI
 315 scenarios in CESM1 and CESM2 (Figs. 5 and 6) exhibits a similar cold-tongue pattern (typical of the
 316 North Pacific) as in the historical period. A lower contrast between the cold-tongue pattern and its
 317 surroundings is observed under SSP5-8.5 (Fig. 6b), which is effectively compensated by the
 318 geoengineering scenarios of SSP5-8.5-SAI through a significant SST decrease over middle North
 319 Pacific (Fig. 6c and 6f) since there is no significant change between SAI and historical maps (Fig. 6e).
 320 There is an excessive eastward expansion of the cold-tongue pattern with cooler temperatures under
 321 the SAI scenario as simulated by the CESM1 (Fig. 5c), which is due to the significant cooling of the
 322 water in the outside of the cold-tongue pattern imposed by the SO₂ injection (Fig. 5e-f).

323

324

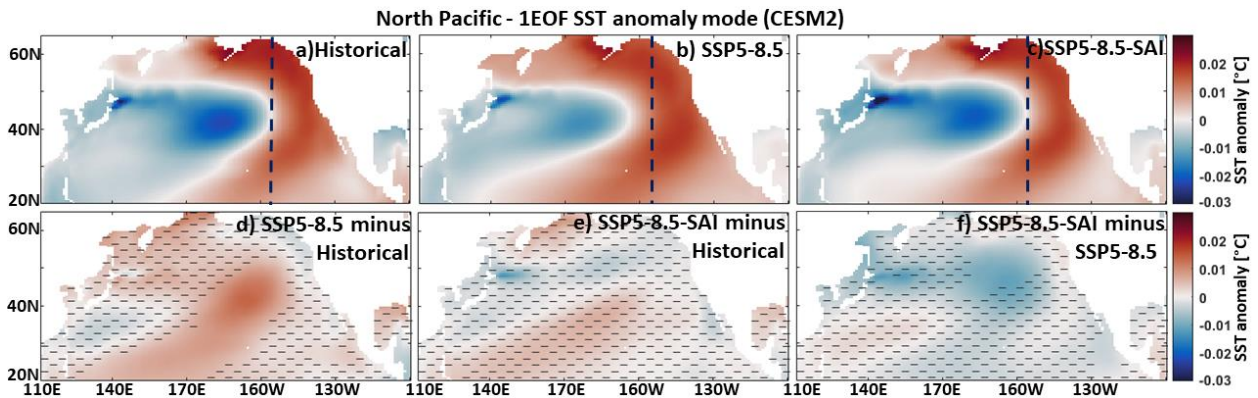


325

326

Figure 5. As Fig. 3 but across the North Pacific relates to the PDO index.

327



328

329

Figure 6. As in Fig. 5, but for CESM2.

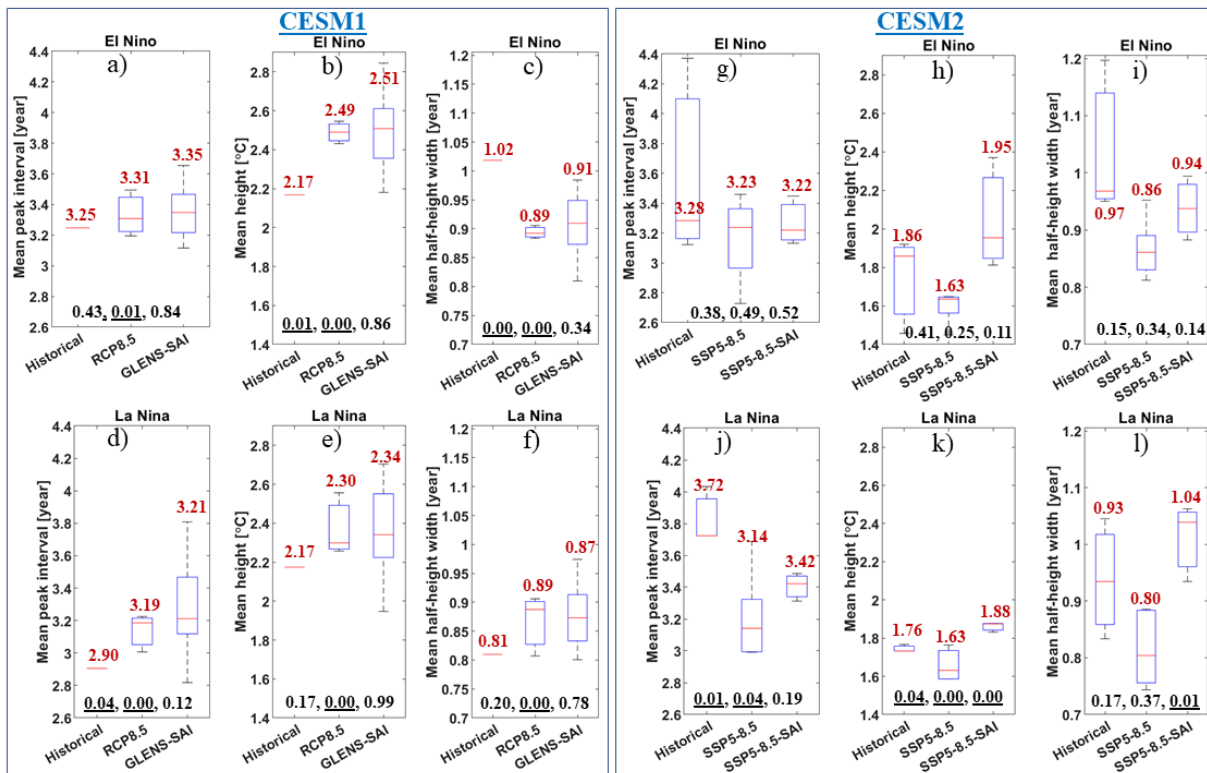
330

331 3.2. Temporal evolution of indices

332 Figure 7 displays the projected changes in the El Niño and La Niña episodes in the ENSO index under
 333 global warming and SAI. The global warming scenario simulated by CEMS2 tends to reduce the time
 334 between, as well as the intensity and duration of the La Niña episodes compared to the historical
 335 conditions, but El Niño shows no significant changes. Frequency increases in both El Niño and La
 336 Niña episodes were suggested in earlier climate simulations e.g., Fredriksen et al. (2020), Cai et al.
 337 (2014) and Yun et al. (2021) for El Niño, and Cai et al. (2015) for La Niña. In contrast, using CESM1,
 338 the characteristic changes of El Niño are stronger than that of La Niña and the El Niño intensity
 339 significantly increases while its duration decreases relative to historical period. The La Niña intensity
 340 significantly increases but other characteristics show no significant changes under RCP8.5.

341 For CESM2, although the SAI is mostly accompanied by a slight decrease in the median of El Niño/La
 342 Niña characteristics towards their historical value, its effect on global warming imposed-changes is
 343 only statistically significant for the intensity and duration of La Niña events. For the CESM2 SAI

344 experiment, there are no significant differences in El Niño characteristics as with the GHG forcing
 345 experiment. In contrast La Niña peak intervals, height (i.e., intensity), and width (i.e., duration)
 346 characteristics are significantly different from GHG forcing and reverse the direction of changes
 347 imposed by GHG. For CESM1, there are no significant differences between the results from RCP8.5
 348 and GLENS-SAI scenarios.
 349



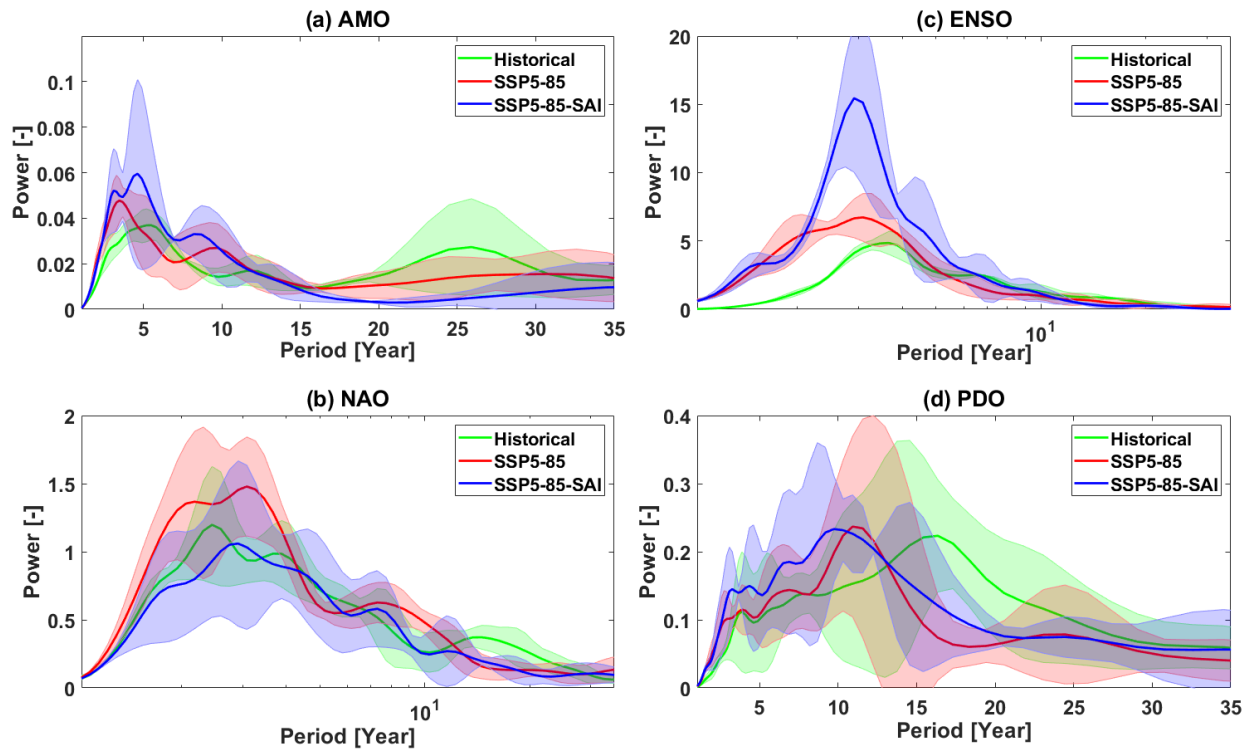
350
 351 **Figure 7.** The projected changes in the mean peak interval, height, and half-height width of El Niño
 352 and La Niña events for global warming (RCP8.5 and SSP5-8.5) and SAI (GLENS-SAI and SSP5-8.5-
 353 SAI) scenarios simulated by CESM1 (panels a-f) and CESM2 (panel g-l). The median for each
 354 experiment is denoted by the red line, the upper (75th) and lower (25th) quartiles by the top and
 355 bottom of the box and ensemble limits by the whisker extents. The values labeled in red on each
 356 box show their median. The three values shown at bottom of each sub-plot refer to the p-values
 357 obtained from the statistical t-test between historical and global warming, historical and SAI, and
 358 global warming and SAI, respectively. Values underlined are significant (i.e., $p < 0.05$).
 359

360 Another way to illustrate the temporal evolution of signals is by using the power spectrum. Figures
 361 8 and S6 compare the changes in temporal variability of each climate indices (AMO, NAO, ENSO, and
 362 PDO) using the global power spectrums of CWTs under the global warming and SAI scenarios
 363 simulated by CESM2, excluding CESM1 outputs as there is just a single ensemble member for CESM1
 364 historical data over a short 1980-2009 period. In CESM1, the signals longer than decadal, which are
 365 the most energetic modes in observations of the PDO (Mantua and Hare, 2002) and AMO (Enfield et

366 al., 2001), cannot be captured in the historical simulations owing to their short simulation period
367 (1980-2009). As an example, Fig. S5 shows the ENSO CWTs and their global power spectrums for
368 historical, SSP5-8.5, and SSP5-8.5-SAI scenarios.

369 The inter-annual modes of AMO, NAO, and ENSO are preserved under both global warming and SAI.
370 For the decadal periodicities, SAI accentuates AMO changes induced by GHG (Fig. 8a). For example,
371 the dominant modes at 20-30-year of the AMO, observed during the historical period, show no
372 significant changes under global warming; however, they vanish under SAI. The decadal 10-20-years
373 mode of the historical NAO is not preserved in the global warming scenario nor with SAI (Fig. 8b).
374 For ENSO, the dominant historical inter-annual modes show no significant change under both global
375 warming and SAI, except that its power under SAI is stronger (Fig. 8c). The dominant modes at 10-
376 20-years, observed in historical PDO, are not present in both the SSP5-8.5 and SAI simulations, and
377 the latter two are similar to each other (Fig. 8d). In contrast with the historical period in which the
378 dominant modes of PDO occur in the 10-20-year band, the dominant modes under global warming
379 (i.e., SSP5-8.5) and SAI (i.e., SSP5-8.5-SAI) shifts to a lower mode at the ~8-13-year period. The PDO
380 shift to a higher frequency with decadal variability weakness, observed under global warming, was
381 also earlier demonstrated by Fang et al. (2014) with a previous generation of the climate model, the
382 Fast Ocean Atmosphere Model (FOAM) used in IPCC AR4 experiments. Likewise, the PDO timescale
383 has been simulated to decrease from ~20 to ~12 years under global warming (Fedorov et al., 2020),
384 possibly because of changes in the phase speed of internal Rossby waves and ocean stratification
385 (Zhang and Delworth, 2016).

386 We further analyzed the concatenated series from the available members for each scenario using
387 CESM2 to statistically capture the low frequency cycles with better reliability. Figure S6 summarizes
388 the CWT global power spectrums for AMO, NAO, ENSO, and PDO. The results, on the whole, are
389 compatible with those shown in Fig. 8.



390

391 **Figure 8.** The CWT global power spectra obtained for the indices of AMO (a), NAO (b), ENSO (c),
 392 and PDO (d) under SSP5-8.5 and SSP5-8.5-SAI relative to the historical results based on CESM2 for
 393 the periods of 1850-2014. Shading in each curve shows the across-ensemble range. The x-axis in
 394 NAO and ENSO graphs is on logarithmic scale.

395

396 4. Discussion

397 4.1. Caveats to interpretation

398 Caution is required when interpreting the results from this study with regard to real-world
 399 variability. Although CESM2 is highly rated among existing climate models, large model-observation
 400 differences are nonetheless present (Fasullo, 2020). Model-observation differences are larger in the
 401 earlier CESM1 version than in CESM2. For example, CESM1 exhibited a Subtropical (Azores) high
 402 anomaly (related to NAO) that was too weak but its representation is improved in CESM2 (Simpson
 403 et al., 2020). We also find large differences in amplitude and variance of climate indices simulated by
 404 both CESM1 and CESM2 relative to the observations over the 1980-2009 period. The amplitude of
 405 the dominant EOF of the ENSO-related SST-anomaly modeled in both CESM1 and CESM2 is about
 406 twice the observations for the historical (1980-2009) period (Figs. S4 and S7). Figure S7 further
 407 shows NAO and PDO dominant mode amplitudes are lower in the model projections than in
 408 observations over the historical period. Additionally, the ENSO-associated SST anomaly pattern in
 409 the tropical Pacific shows an excessive westward extension under both CESM1 and CESM2 (Fig. S4).

410 These limitations mirror those by Capotondi et al. (2020) for CESM2 in simulating the ENSO, who
411 suggested further work to illuminate how the physical parameterizations impact the key ENSO
412 feedback. Additionally, although CESM2 simulates the pattern of the summer and winter NAO well
413 over the historical period 1979-2014, the large uncertainties in specific members and in the historical
414 observations mean it is difficult to be quantitative about this (Simpson et al., 2020). However, CESM1
415 tends to underestimate the observed SST fluctuations in the Atlantic, leading to an underestimation
416 of the forced response (Undorf et al., 2018).

417 CMIP models tend to systematically underestimate the low-frequency signals (i.e., PDO) in the North
418 Pacific (Fasullo et al., 2020), owing in part to an imperfect modeling of decadal-scale structures in
419 these simulations (Masson-Delmotte et al., 2021). Compared to observational estimates, the decadal
420 variability in the subpolar North Atlantic SST appears to be slightly intensified through CMIP6
421 (Masson-Delmotte et al., 2021). How well we, therefore, can potentially capture forthcoming changes
422 in climate indices' variability will be restricted by how good each model simulations are (Gabriel and
423 Robock, 2015).

424 The second limitation is disparities in the length of records (30 (165) years for the historical period
425 from CESM1 (CESM2), roughly ~90 years for GHG emissions, and ~80 years for SAI scenarios) may
426 hinder the direct comparison of climate indices behavior between historical and future climate
427 scenarios of global warming and SAI; and thus, the number of El Niño/La Niña events as well as the
428 significance of the longer periodicities (i.e., decadal and inter-decadal) in power spectrums.
429 Furthermore, these records explore variability within the statistical assumptions of the methods,
430 which may not be robust for non-stationary time series where the normality and independence
431 assumptions inherent in the wavelet and t-tests would not strictly hold. We are limited to the
432 available simulations, and a 3-member ensemble for SAI under CESM2 is inherently weaker than 20-
433 member ensembles under CESM1. CESM1 has a shorter 30-year historical period from 1980 to 2009
434 which could not capture the longer than decadal variability modes of the teleconnection patterns. Yet
435 another limitation arises from the relatively low spatial resolution of the models which may affect
436 the spatial SST anomaly patterns. Furthermore, Holmes et al. (2019) pointed out the models are too
437 low resolution to resolve ocean eddies, which substantially contribute to ENSO irregularity and
438 predictability. The absence of the eddy process may also be associated with bias in spatial patterns
439 and other ENSO characteristics (Bellenger et al., 2014) in the CMIP models (Cai et al., 2021). Global
440 high-horizontal resolution climate models have been indicated to significantly improve the ocean-
441 atmosphere circulations such as ENSO (Masson et al., 2012). As an example, Haarsma et al. (2016)
442 pointed out that the High Resolution Model Intercomparison Project for CMIP6 improves the

443 understanding of the climate teleconnection patterns of large-scale circulations such as ENSO, NAO,
444 and PDO, which suggests that running these high-resolution models with SAI scenario would be
445 worthwhile.

446

447 **4.2. Implications for climate stability**

448 Teleconnection signals represent emergent properties of the non-linear climate system. The
449 behavior of the climate teleconnection patterns can be characterized via its oscillations. In its
450 simplest form, a stable pattern would represent a fixed point or a periodic oscillation, but with real
451 non-linear systems, a quasi-periodic oscillation over specific frequency bands is more likely (e.g., Ghil
452 et al., 2002). These quasi-periodic characteristic frequencies may change smoothly over time in a
453 linear system but may proceed towards chaotic solutions via frequency doubling in non-linear
454 systems. Moron et al. (1998) suggested that ENSO crossed a threshold in the early 1960s, and the
455 periodicity of the seasonally forced climatic oscillator increased abruptly. Notably, a concomitant
456 increase in the variance of the decadal band is consistent with abrupt frequency doubling. This can
457 be expected in non-linear systems as the energy in the system is raised, progressing along the
458 pathway towards chaotic behavior and hence less predictability on decadal timescales.

459 The impact of SAI on the energetics of the coupled system are to offset the GHG increases by design.
460 Hence, we might expect that SAI could therefore reduce or stop the progression towards chaotic
461 behavior. However, the real climate system is far more complex than a simple energy balance
462 calculation. SAI increases stratospheric heating (Visioni et al., 2020), and this leads to tropospheric
463 changes, especially in winds (Gertler et al., 2020), and tropical circulation (Cheng et al., 2022).
464 Furthermore, the large heat reservoir of the global ocean has been out of equilibrium with the
465 atmosphere for centuries of anthropogenic GHG emissions, and this excess heat cannot be dissipated
466 by SAI within the timeframe in the simulations. So, we may expect SAI to, at best, imperfectly reverse
467 the effects of GHG on teleconnections.

468 Ocean stratification (ocean buoyancy frequency) and the baroclinic Rossby wave in the North Pacific
469 play significant roles in SST amplitude and PDO cycles since enhanced ocean buoyancy frequency
470 speeds up the Rossby waves, and so the decadal and longer cycle weakening accompanies higher PDO
471 frequency (Fang et al., 2014). Ocean stratification changes predominantly in response to changes in
472 surface temperature and salinity (Fang et al., 2014). The North Atlantic and the northeast Pacific are
473 projected to be among those areas with the greatest stratification changes under global warming in
474 the second-half of the 21st century (Capotondi et al. 2012).

475 While SAI effectively reverses the changes in the spatial patterns under GHG forcing across the North
476 Atlantic (i.e., AMO) and North Pacific (i.e., PDO) and compensates for modest changes in the
477 characteristics of the El Niño and La Niña episodes (related to the tropical Pacific), it does not
478 effectively suppress the projected changes in decadal (~10-20-year) variability of circulations
479 imposed by global warming. Anthropogenic aerosols intensify the inter-annual variability
480 (particularly in ENSO) but weaken the longer than 10-year signals of the ocean-atmosphere
481 circulations, compatible with the multiyear to decadal variations in PDO (Hua et al., 2018). SAI
482 involves aerosols in the stratosphere not the troposphere, so the effects will be different, not least
483 because of stratospheric heating (Visoni et al., 2020). The cold-tong patterns in the mid-latitude of
484 both North Atlantic and North Pacific tend to have an excess eastward extension under SAI, in line
485 with the second-phase of the North Pacific response to large volcanic eruptions (Wang et al., 2012),
486 which are better analogues for SAI.

487 Whether the climate system in the model is representative of the earth can be diagnosed to some
488 extent by comparison of the historical simulation with observations. As noted in Section 4.1 both
489 CESM versions do present differences from observations, so they are not perfect. All climate models
490 are unavoidably uncertain (Knutti et al., 2002), mostly because of the imperfect understanding of
491 many of the interplays and feedbacks within the climate system (Jun et al., 2008). Previous analysis
492 of ENSO under SAI found no significant changes (Gabriel & Robock, 2015), but they used different
493 models with widely varying fidelity of modeled ENSO to observations, and much smaller simulated
494 quantities of SO₂ with the relatively modest RCP4.5 emissions scenario as a baseline. Furthermore,
495 in the only previous assessment of ENSO under SAI, by Gabriel and Robock (2015), SAI simulations
496 may not have been long enough to detect changes. The large 20-member ensemble of GLENS used in
497 this study may overcome this limitation, especially for short-period indices, since this represents
498 ~1600 model-years.

499 Changes in climate teleconnection patterns can indicate significant changes in the forcing. Such
500 changes are seen in time series analysis of teleconnection indices in the real world that coincide with
501 increased GHG (Tsonis et al., 2007; Wang et al., 2009). Wang et al (2009) note that regime shifts in
502 system behavior in the observations occurred when North Pacific and North Atlantic patterns
503 increase their coupling, and the key instigator is the NAO. The historical NAO's decadal mode which
504 vanished under global warming in our analyses is not restored by the simulated SAI.

505 The North Atlantic is an atypical region under SAI. The declines in heat transported northwards by
506 the AMOC under GHG forcing are, to great extent, reversed under all kinds of SRM including SAI (Xie
507 et al., 2022). Thus, great differences exist in SST and air/ocean heat flux between SAI and GHG

508 climates in the North Atlantic (Yue et al., 2021). If regime shifts occur when North Atlantic and Pacific
509 oceans increase their coupling, and if the decline in AMOC under GHG forcing decreases coupling
510 between the basins, then SAI may act to promote regime shift by reversing a decline in AMOC.
511 Many authors have noted that explosive volcanism, in some ways a natural analogue for SAI, is
512 accompanied by a positive episode of the NAO (e.g., Robock, 2000). Furthermore, in the extreme
513 scenario of SAI being done such that temperatures are actually decreased then projected
514 strengthening of AMOC occurs (Tjiputra et al., 2016). However, it is also possible that regime shifts
515 induced by GHG forcing and the large temperature feedbacks they induce may dominate impacts over
516 those fairly subtle regime shifts in climate teleconnection patterns.

517

518 **5. Conclusions**

519 This study delivers a first overview of SAI response on the large-scale ocean-atmosphere circulations
520 of AMO, NAO, ENSO, and PDO using experiments based on CESM1(WACCM) and CESM2(WACCM6)
521 that apply stratospheric aerosol intervention through the injection of sulfur into the stratosphere,
522 GLENS-SAI and SSP5-8.5-SAI, respectively. The impacts of these interventions are assessed against
523 historical (1980-2009 for both the models and 1850-2014 for CESM2 in some analyses) and
524 projections under RCP8.5 and SSP5-85 (for the GLENS-SAI and SSP5-8.5-SAI, respectively). We found
525 that SAI effectively reverses the global warming-imposed changes in the variance of the leading EOF
526 SST anomaly associated with AMO, ENSO, and PDO. The SAI also effectively suppresses the changes
527 in the spatial patterns of the EOF SST anomaly across the North Atlantic (i.e., AMO) and North Pacific
528 (i.e., PDO). A decrease in the contrast between the cold-tongue pattern and its surroundings in the
529 North Pacific is further projected under GHG induced global warming, which the SAI successfully
530 restored.

531 CESM2 simulations suggest that increasing GHG emissions are accompanied by a modest increase in
532 the frequency of the El Niño and La Niña episodes but a modest decrease in their intensity and
533 duration. The SAI scenario effectively compensates for these changes.

534 In contrast to the impact of the SAI on the spatial patterns of the climate indices of AMO, PDO, and
535 ENSO, the SAI scenario does not effectively suppress the projected changes in decadal (~10-20-year)
536 variability imposed by global warming. The decadal variability modes of all the historical climate
537 indices (except for Atlantic-based indices under SSP5-8.5) are not preserved in the GHG warming
538 scenario and the SAI does not restore them.

539 Furthermore, compared to the historical 1850-2014 period in CESM2, SAI is projected to accentuate
540 AMO and have no effective impact on NAO at decadal frequencies. Unlike the historical period in

541 which the long-period dominant modes of PDO occur in the 10-20-year band, the dominant modes
542 under global warming are reduced to ~8-13-years, and the SAI does not restore them.
543 The results exhibited here are particular to these types of future global warming scenarios and the
544 details of the SAI application, which deal with an extreme scenario of GHG emissions and continuous
545 increases in sulfur emissions. Furthermore, the findings are from ensemble members from just two
546 closely related models. Caution is warranted due to the model-observation differences, disparities in
547 the record length of the historical period compared to future climate scenarios, and the low spatial
548 resolution of the models. Nevertheless, our study does detect changes in climate teleconnection
549 signals, and hence underlying climate system dynamics under SAI when decomposed using EOF and
550 wavelet analyses.

551

552 **Acknowledgments:**

553 We appreciate the financial support from The World Academy of Sciences (TWAS) under grant no:
554 4500443035. We further thank Gary Strand from NCAR for his help in accessing the CESM1 model
555 outputs. Tan Mou Leong provided helpful comments and suggestions on the manuscript.

556

557 **Competing interests:**

558 We confirm that there is no conflict of interest among the authors of this manuscript.

559

560 **Data availability:**

561 The data for CESM1 and CESM2 simulations are publicly available via their websites:
562 <http://www.cesm.ucar.edu/projects/community-projects/GLENS/> (DOI: 10.5065/D6JH3JXX) and
563 <https://esgf-node.llnl.gov/search/cmip6/>.

564

565

566 **Author contribution:**

567 A. R.: Coordinated to analysis and the graphics of various figures and the manuscript preparation; Kh.
568 K. and S. T.: conceptualization and preparing the data; J. M. conceptualized and coordinated the
569 interpretation and discussion for various sections. All authors contributed to the discussion and
570 writing.

571

572

573

574 **References:**

- 575 Addison, P. S.: Introduction to redundancy rules: the continuous wavelet transform comes of
576 age, *Philosophical Transactions of the Royal Society A: Mathematical, Physical and*
577 *Engineering Sciences*, 376(2126), 20170258, <https://doi.org/10.1098/rsta.2017.0258>,
578 2018.
- 579 Abdelmoaty, H. M., Papalexiou, S. M., Rajulapati, C. R., and AghaKouchak, A.: Biases beyond the mean
580 in CMIP6 extreme precipitation: A global investigation, *Earth's Future*, 9(10),
581 e2021EF002196, <https://doi.org/10.1029/2021EF002196>, 2021.
- 582 An, S. I., and Wang, B.: Inter-decadal change of the structure of the ENSO mode and its impact on the
583 ENSO frequency, *Journal of Climate*, 13(12), 2044-2055, [https://doi.org/10.1175/1520-0442\(2000\)013<2044:ICOTSO>2.0.CO;2](https://doi.org/10.1175/1520-0442(2000)013<2044:ICOTSO>2.0.CO;2), 2000.
- 585 Bellenger, H., Guilyardi, É., Leloup, J., Lengaigne, M., and Vialard, J.: ENSO representation in climate
586 models: From CMIP3 to CMIP5, *Climate Dynamics*, 42(7), 1999-2018,
587 <https://doi.org/10.1007/s00382-013-1783-z>, 2014.
- 588 Cai, W., Santoso, A., Collins, M., Dewitte, B., Karamperidou, C., Kug, J. S., ... and Zhong, W.: Changing El
589 Niño–Southern Oscillation in a warming climate. *Nature Reviews Earth & Environment*, 2(9),
590 628-644, <https://doi.org/10.1038/s43017-021-00199-z>, 2021.
- 591 Cai, W., Wang, G., Santoso, A., McPhaden, M. J., Wu, L., Jin, F. F., ... and Guilyardi, E.: Increased frequency
592 of extreme La Niña events under greenhouse warming, *Nature Climate Change*, 5(2), 132-
593 137, <https://doi.org/10.1038/nclimate2492>, 2015.
- 594 Cai, W., Borlace, S., Lengaigne, M., Van Rensch, P., Collins, M., Vecchi, G., ... and Jin, F. F.: Increasing
595 frequency of extreme El Niño events due to greenhouse warming, *Nature climate*
596 *change*, 4(2), 111-116, <https://doi.org/10.1038/nclimate2100>, 2014.
- 597 Capotondi, A., Deser, C., Phillips, A. S., Okumura, Y., & Larson, S. M.: ENSO and Pacific decadal
598 variability in the Community Earth System Model version 2, *Journal of Advances in Modeling*
599 *Earth Systems*, 12(12), e2019MS002022, <https://doi.org/10.1029/2019MS002022>, 2020.
- 600 Capotondi, A., & Sardeshmukh, P. D.: Is El Niño really changing?, *Geophysical Research*
601 *Letters*, 44(16), 8548-8556, <https://doi.org/10.1002/2017GL074515>, 2017.
- 602 Capotondi, A., Alexander, M. A., Bond, N. A., Curchitser, E. N., and Scott, J. D., Enhanced upper ocean
603 stratification with climate change in the CMIP3 models, *Journal of Geophysical Research:*
604 *Oceans*, 117(C4), <https://doi.org/10.1029/2011JC007409>, 2012.

605 Chen, X., and Tung, K. K.: Global-mean surface temperature variability: Space–time perspective from
606 rotated EOFs, *Climate Dynamics*, 51(5), 1719-1732, [https://doi.org/10.1007/s00382-017-](https://doi.org/10.1007/s00382-017-3979-0)
607 [3979-0](https://doi.org/10.1007/s00382-017-3979-0), 2018.

608 Cheng, W., MacMartin, D. G., Kravitz, B., Vioni, D., Bednarz, E. M., Xu, Y., ... and Deng, X.: Changes in
609 Hadley circulation and intertropical convergence zone under strategic stratospheric aerosol
610 geoengineering, *npj Climate and Atmospheric Science*, 5(1), 32,
611 <https://doi.org/10.1038/s41612-022-00254-6>, 2022.

612 Cheng, L., Trenberth, K. E., Fasullo, J., Boyer, T., Abraham, J., and Zhu, J.: Improved estimates of ocean
613 heat content from 1960 to 2015, *Science Advances*, 3(3), e1601545,
614 <https://doi.org/10.1126/sciadv.1601545>, 2017.

615 Cook, B. I., Mankin, J. S., Marvel, K., Williams, A. P., Smerdon, J. E., and Anchukaitis, K. J.: Twenty-first
616 century drought projections in the CMIP6 forcing scenarios, *Earth's Future*, 8(6),
617 e2019EF001461, <https://doi.org/10.1029/2019EF001461>, 2020.

618 Dagon, K., and Schrag, D. P.: Exploring the effects of solar radiation management on water cycling in
619 a coupled land–atmosphere model. *Journal of Climate*, 29(7), 2635-2650,
620 <https://doi.org/10.1175/JCLI-D-15-0472.1>, 2016.

621 Danabasoglu, G., Lamarque, J. F., Bacmeister, J., Bailey, D. A., DuVivier, A. K., Edwards, J., ... and Strand,
622 W. G.: The community earth system model version 2 (CESM2), *Journal of Advances in*
623 *Modeling Earth Systems*, 12(2), e2019MS001916, <https://doi.org/10.1029/2019MS001916>,
624 2020.

625 Enfield, D. B., Mestas-Nuñez, A. M., and Trimble, P. J.: The Atlantic multidecadal oscillation and its
626 relation to rainfall and river flows in the continental US, *Geophysical Research*
627 *Letters*, 28(10), 2077-2080, <https://doi.org/10.1029/2000GL012745>, 2001.

628 Eyring, V., Bony, S., Meehl, G. A., Senior, C. A., Stevens, B., Stouffer, R. J., and Taylor, K. E.: Overview of
629 the Coupled Model Intercomparison Project Phase 6 (CMIP6) experimental design and
630 organization, *Geoscientific Model Development*, 9(5), 1937-1958,
631 <https://doi.org/10.1029/2000GL012745>, 2016.

632 Fang, C., Wu, L., and Zhang, X.: The impact of global warming on the Pacific Decadal Oscillation and
633 the possible mechanism, *Advances in Atmospheric Sciences*, 31(1), 118-130,
634 <https://doi.org/10.1007/s00376-013-2260-7>, 2014.

635 Fasullo, J. T. and Richter, J. H.: Scenario and Model Dependence of Strategic Solar Climate Intervention
636 in CESM, *EGUsphere* [preprint], <https://doi.org/10.5194/egusphere-2022-779>, 2022.

637 Fasullo, J. T., Phillips, A. S., and Deser, C.: Evaluation of leading modes of climate variability in the
638 CMIP archives, *Journal of Climate*, 33(13), 5527-5545, [https://doi.org/10.1175/JCLI-D-19-](https://doi.org/10.1175/JCLI-D-19-1024.1)
639 [1024.1](https://doi.org/10.1175/JCLI-D-19-1024.1), 2020.

640 Fedorov, A. V., Hu, S., Wittenberg, A. T., Levine, A. F., and Deser, C.: ENSO Low-Frequency Modulation
641 and Mean State Interactions, *El Niño Southern Oscillation in a changing climate*, 173-198,
642 <https://doi.org/10.1002/9781119548164.ch8>, 2020.

643 Fedorov, A. V., and Philander, S. G.: A stability analysis of tropical ocean–atmosphere interactions:
644 Bridging measurements and theory for El Niño, *Journal of Climate*, 14(14), 3086-3101,
645 [https://doi.org/10.1175/1520-0442\(2001\)014<3086:ASAOTO>2.0.CO;2](https://doi.org/10.1175/1520-0442(2001)014<3086:ASAOTO>2.0.CO;2), 2001.

646 Field, C. B., and Barros, V. R. (Eds.): *Climate change 2014–Impacts, adaptation and vulnerability:*
647 *Regional aspects*, Cambridge University Press, 2014.

648 Fredriksen, H. B., Berner, J., Subramanian, A. C., and Capotondi, A.: How does El Niño–Southern
649 Oscillation change under global warming—A first look at CMIP6, *Geophysical Research*
650 *Letters*, 47(22), e2020GL090640, <https://doi.org/10.1029/2020GL090640>, 2020.

651 Gabriel, C. J., and Robock, A.: Stratospheric geoengineering impacts on El Niño/Southern
652 Oscillation, *Atmospheric Chemistry and Physics*, 15(20), 11949-11966,
653 <https://doi.org/10.5194/acp-15-11949-2015>, 2015.

654 Gertler, C. G., O’Gorman, P. A., Kravitz, B., Moore, J. C., Phipps, S. J., and Watanabe, S.: Weakening of the
655 extratropical storm tracks in solar geoengineering scenarios, *Geophysical Research*
656 *Letters*, 47(11), e2020GL087348, <https://doi.org/10.1029/2020GL087348>, 2020.

657 Ghil, M., Allen, M. R., Dettinger, M. D., Ide, K., Kondrashov, D., Mann, M. E., ... and Yiou, P.: Advanced
658 spectral methods for climatic time series, *Reviews of geophysics*, 40(1), 3-1,
659 <https://doi.org/10.1029/2000RG000092>, 2002.

660 Greene, C. A., Thirumalai, K., Kearney, K. A., Delgado, J. M., Schwanghart, W., Wolfenbarger, N. S., ... and
661 Blankenship, D. D.: The climate data toolbox for MATLAB, *Geochemistry, Geophysics,*
662 *Geosystems*, 20(7), 3774-3781, <https://doi.org/10.1029/2019GC008392>, 2019.

663 Grinsted, A., Moore, J.C., and Jevrejeva, S.: Application of the cross wavelet transform and wavelet
664 coherence to geophysical time series, *Nonlinear Proc. Geoph.* 11 (5-6), 561-566,
665 <https://doi.org/10.5194/npg-11-561-2004>, 2004.

666 Haarsma, R. J., Roberts, M. J., Vidale, P. L., Senior, C. A., Bellucci, A., Bao, Q., Chang, P., Corti, S., Fučkar,
667 N. S., Guemas, V., von Hardenberg, J., Hazeleger, W., Kodama, C., Koenigk, T., Leung, L. R., Lu,
668 J., Luo, J.-J., Mao, J., Mizielinski, M. S., Mizuta, R., Nobre, P., Satoh, M., Scoccimarro, E., Semmler,
669 T., Small, J., and von Storch, J.-S.: High Resolution Model Intercomparison Project

670 (HighResMIP v1.0) for CMIP6, *Geosci. Model Dev.*, 9, 4185–4208,
671 <https://doi.org/10.5194/gmd-9-4185-2016>, 2016.

672 Holmes, R. M., McGregor, S., Santoso, A., and England, M. H.: Contribution of tropical instability waves
673 to ENSO irregularity, *Climate Dynamics*, 52(3), 1837-1855,
674 <https://doi.org/10.1007/s00382-018-4217-0>, 2019.

675 Hu, Z. Z., and Wu, Z.: The intensification and shift of the annual North Atlantic Oscillation in a global
676 warming scenario simulation, *Tellus A: Dynamic Meteorology and Oceanography*, 56(2), 112-
677 124, <https://doi.org/10.3402/tellusa.v56i2.14403>, 2004.

678 Hua, W., Dai, A., and Qin, M.: Contributions of internal variability and external forcing to the recent
679 Pacific decadal variations, *Geophysical Research Letters*, 45(14), 7084-7092,
680 <https://doi.org/10.1029/2018GL079033>, 2018.

681 Intergovernmental Panel on Climate Change (IPCC): Working Group I Contribution to the Sixth
682 Assessment Report (AR6), *Climate Change 2021: The Physical Science Basis*, 2021. Available
683 online: <https://www.ipcc.ch/assessment-report/ar6/>, 2007.

684 Joyce, T. M.: One hundred plus years of wintertime climate variability in the eastern United States, *J.*
685 *Clim.*, 15, 1076–1086, [https://doi.org/10.1175/1520-
686 0442\(2002\)015<1076:OHPYOW>2.0.CO;2](https://doi.org/10.1175/1520-0442(2002)015<1076:OHPYOW>2.0.CO;2), 2002.

687 Knutti, R., Stocker, T. F., Joos, F., and Plattner, G. K.: Constraints on radiative forcing and future climate
688 change from observations and climate model ensembles, *Nature*, 416(6882), 719-723,
689 <https://doi.org/10.1038/416719a>, 2002.

690 Jun, M., Knutti, R., and Nychka, D. W.: Spatial analysis to quantify numerical model bias and
691 dependence: how many climate models are there?, *Journal of the American Statistical*
692 *Association*, 103(483), 934-947, <https://doi.org/10.1198/016214507000001265>, 2008.

693 Kravitz, B., MacMartin, D. G., Mills, M. J., Richter, J. H., Tilmes, S., Lamarque, J. F., Tribbia, J. J. and Vitt,
694 F.: First simulations of designing stratospheric sulfate aerosol geoengineering to meet
695 multiple simultaneous climate objectives, *Journal of Geophysical Research: Atmospheres*,
696 122, 12,616–12,634, <https://doi.org/10.1002/2017JD026874>, 2017.

697 Kravitz, B., Caldeira, K., Boucher, O., Robock, A., Rasch, P. J., Alterskjaer, K., ... and Yoon, J. H.: Climate
698 model response from the geoengineering model intercomparison project (GeoMIP), *Journal*
699 *of Geophysical Research: Atmospheres*, 118(15), 8320-8332,
700 <https://doi.org/10.1002/jgrd.50646>, 2013.

701 Latif, M., and Keenlyside, N. S.: El Niño/Southern Oscillation response to global warming, Proceedings
702 of the National Academy of Sciences, 106(49), 20578-20583,
703 <https://doi.org/10.1073/pnas.0710860105>, 2009.

704 Mantua, N., and Hare, S.: The Pacific Decadal oscillation, *J. Oceanogr.* 58 (1), 35–44.
705 <http://dx.doi.org/10.1023/A:1015820616384>, 2002.

706 Mantua, N. J., Hare, S. R., Zhang, Y., Wallace, J. M., and Francis, R. C.: A Pacific interdecadal climate
707 oscillation with impacts on salmon production, *Bulletin of the American Meteorological*
708 *Society*, 78(6), 1069-1080, [https://doi.org/10.1175/1520-
709 0477\(1997\)078<1069:APICOW>2.0.CO;2](https://doi.org/10.1175/1520-0477(1997)078<1069:APICOW>2.0.CO;2), 1997.

710 Masson-Delmotte, V., Zhai, P., Pirani, A., Connors, S. L., Péan, C., Berger, S., ... and Zhou, B.: Climate
711 change 2021: the physical science basis, Contribution of working group I to the sixth
712 assessment report of the intergovernmental panel on climate change, 2,
713 <https://10.1017/9781009157896>, 2021.

714 Masson, S., Terray, P., Madec, G., Luo, J. J., Yamagata, T., and Takahashi, K.: Impact of intra-daily SST
715 variability on ENSO characteristics in a coupled model, *Climate dynamics*, 39(3), 681-707,
716 <https://doi.org/10.1007/s00382-011-1247-2>, 2012.

717 Mills, M. J., Richter, J. H., Tilmes, S., Kravitz, B., MacMartin, D. G., Glanville, A. A., Tribbia, J. J., Lamarque,
718 J. F., Vitt, F., Schmidt, A. and Gettelman, A.: Radiative and chemical response to interactive
719 stratospheric sulfate aerosols in fully coupled CESM1(WACCM), *Journal of Geophysical*
720 *Research: Atmospheres*, 122, 13,061–13,078, <https://doi.org/10.1002/2017JD027006>,
721 2017.

722 Meinshausen, M., Lewis, J., McGlade, C., Gütschow, J., Nicholls, Z., Burdon, R., ... and Hackmann, B.:
723 Realization of Paris Agreement pledges may limit warming just below 2°
724 C, *Nature*, 604(7905), 304-309, <https://doi.org/10.1038/s41586-022-04553-z>, 2022.

725 Moore, J. C., Yue, C., Zhao, L., Guo, X., Watanabe, S., and Ji, D.: Greenland ice sheet response to
726 stratospheric aerosol injection geoengineering, *Earth's Future*, [https://doi.org/10.1029/
727 2019EF001393](https://doi.org/10.1029/2019EF001393), 2019.

728 Moore, J. C., Rinke, A., Yu, X., Ji, D., Cui, X., Li, Y., Alterskjaer, K., Kristjánsson, J. E., Muri, H., Boucher, O.
729 and Huneus, N.: Arctic sea ice and atmospheric circulation under the GeoMIP G1 scenario,
730 *Journal of Geophysical Research: Atmospheres*, 119, 567–583,
731 <https://doi.org/10.1002/2013JD021060>, 2014.

732 Moron, V., Vautard, R., and Ghil, M.: Trends, interdecadal and interannual oscillations in global sea-
733 surface temperatures, *Climate Dynamics*, 14(7), 545-569,
734 <https://doi.org/10.1007/s003820050241>, 1998.

735 Riahi, K., Rao, S., Krey, V., Cho, C., Chirkov, V., Fischer, G., ... and Rafaj, P.: RCP 8.5—A scenario of
736 comparatively high greenhouse gas emissions, *Climatic change*, 109(1), 33-57,
737 <https://doi.org/10.1007/s10584-011-0149-y>, 2011.

738 Robock, A.: Volcanic eruptions and climate, *Reviews of Geophysics*, 38(2), 191-
739 219, <https://doi.org/10.1029/1998RG000054>, 2000.

740 Scafetta, N.: Testing the CMIP6 GCM Simulations versus surface temperature records from 1980-
741 1990 to 2011-2021: High ECS is not supported, *Climate*, 9(11),
742 161, <https://doi.org/10.3390/cli9110161>, 2021.

743 Simpkins, G.: Breaking down the NAO-AO connection, *Nature Reviews Earth & Environment*, 2(2),
744 88-88, <https://doi.org/10.1038/s43017-021-00139-x>, 2021.

745 Simpson, I. R., Bacmeister, J., Neale, R. B., Hannay, C., Gettelman, A., Garcia, R. R., ... and Richter, J. H.:
746 An evaluation of the large-scale atmospheric circulation and its variability in CESM2 and
747 other CMIP models, *Journal of Geophysical Research: Atmospheres*, 125(13),
748 e2020JD032835, <https://doi.org/10.1029/2020JD032835>, 2020.

749 Shukla, J.: Predictability in the midst of chaos: A scientific basis for climate
750 forecasting, *science*, 282(5389), 728-731, <https://doi.org/10.1126/science.282.5389.728>,
751 1998.

752 Sutton, R. T., and Hodson, D. L.: Climate response to basin-scale warming and cooling of the North
753 Atlantic Ocean, *Journal of Climate*, 20(5), 891-907, <https://doi.org/10.1175/JCLI4038.1>,
754 2007.

755 Tilmes, S., MacMartin, D. G., Lenaerts, J. T. M., van Kampenhout, L., Muntjewerf, L., Xia, L., Harrison, C.
756 S., Krumhardt, K. M., Mills, M. J., Kravitz, B., and Robock, A.: Reaching 1.5 and 2.0 °C global
757 surface temperature targets using stratospheric aerosol geoengineering, *Earth Syst. Dynam.*,
758 11, 579-601, <https://doi.org/10.5194/esd-11-579-2020>, 2020.

759 Tilmes, S., Richter, J. H., Kravitz, B., MacMartin, D. G., Mills, M. J., Simpson, I. R., Glanville, A. S., Fasullo,
760 J. T., Phillips, A. S., Lamarque, J. F. and Tribbia, J.: CESM1(WACCM) Stratospheric Aerosol
761 Geoengineering Large Ensemble Project, *Bulletin of the American Meteorological Society*, 99,
762 2361-2371. <https://doi.org/10.1175/BAMSD-17-0267.1>, 2018.

763 Tjiputra, J. F., Grini, A., and Lee, H.: Impact of idealized future stratospheric aerosol injection on the
764 large-scale ocean and land carbon cycles, *Journal of Geophysical Research: Biogeosciences*, 121(1), 2-27, <https://doi.org/10.1002/2015JG003045>, 2016.

766 Trenberth, K. E.: The definition of El Niño, *Bulletin of the American Meteorological Society*, 78(12),
767 2771-2778, [https://doi.org/10.1175/1520-0477\(1997\)078<2771:TDOENO>2.0.CO;2](https://doi.org/10.1175/1520-0477(1997)078<2771:TDOENO>2.0.CO;2), 1997.

768 Tsonis, A. A., Swanson, K., and Kravtsov, S.: A new dynamical mechanism for major climate
769 shifts, *Geophysical Research Letters*, 34(13), <https://doi.org/10.1029/2007GL030288>,
770 2007.

771 Undorf, S., Bollasina, M. A., Booth, B. B. B., and Hegerl, G. C.: Contrasting the effects of the 1850–1975
772 increase in sulphate aerosols from North America and Europe on the Atlantic in the
773 CESM, *Geophysical Research Letters*, 45(21), 11-930,
774 <https://doi.org/10.1029/2018GL079970>, 2018.

775 Visionsi, D., MacMartin, D. G., Kravitz, B., Lee, W., Simpson, I. R., and Richter, J. H.: Reduced poleward
776 transport due to stratospheric heating under stratospheric aerosols
777 geoengineering, *Geophysical Research Letters*, 47(17), e2020GL089470,
778 <https://doi.org/10.1029/2020GL089470>, 2020.

779 Wang, G., Swanson, K. L., and Tsonis, A. A.: The pacemaker of major climate shifts, *Geophysical*
780 *Research Letters*, 36(7), <https://doi.org/10.1029/2008GL036874>, 2009.

781 Wang, C., and Dong, S.: Is the basin-wide warming in the North Atlantic Ocean related to atmospheric
782 carbon dioxide and global warming?, *Geophysical Research Letters*, 37(8),
783 <https://doi.org/10.1029/2010GL042743>, 2010.

784 Wang, T., Otterå, O. H., Gao, Y., and Wang, H.: The response of the North Pacific Decadal Variability to
785 strong tropical volcanic eruptions, *Climate Dynamics*, 39, 2917-2936,
786 <https://doi.org/10.1007/s00382-012-1373-5>, 2012.

787 Watson, A. J., Schuster, U., Bakker, D. C., Bates, N. R., Corbière, A., González-Dávila, M., ... and
788 Wanninkhof, R.: Tracking the variable North Atlantic sink for atmospheric
789 CO₂. *Science*, 326(5958), 1391-1393, <https://doi.org/10.1126/science.1177394>, 2009.

790 Westervelt, D. M., Conley, A. J., Fiore, A. M., Lamarque, J.-F., Shindell, D. T., Previdi, M., Mascioli, N. R.,
791 Faluvegi, G., Correa, G., and Horowitz, L. W.: Connecting regional aerosol emissions reductions
792 to local and remote precipitation responses, *Atmospheric Chemistry and Physics Discussions*,
793 18, 12,461–12,475. <https://doi.org/10.5194/acp-2018-516>, 2018.

794 Xie, M., Moore, J. C., Zhao, L., Wolovick, M., and Muri, H.: Impacts of three types of solar geoengineering
795 on the Atlantic Meridional Overturning Circulation, Atmospheric Chemistry and
796 Physics, 22(7), 4581-4597, <https://doi.org/10.5194/acp-22-4581-2022>, 2022.

797 Yue, C., Schmidt, L. S., Zhao, L., Wolovick, M., and Moore, J. C.: Vatnajökull mass loss under solar
798 geoengineering due to the North Atlantic meridional overturning circulation, Earth's
799 Future, 9(9), e2021EF002052, <https://doi.org/10.1029/2021EF002052>, 2021.

800 Yun, K. S., Lee, J. Y., Timmermann, A., Stein, K., Stuecker, M. F., Fyfe, J. C., and Chung, E. S.: Increasing
801 ENSO–rainfall variability due to changes in future tropical temperature–rainfall
802 relationship, Communications Earth & Environment, 2(1), 1-7,
803 <https://doi.org/10.1038/s43247-021-00108-8>, 2021.

804 Zhang, L., and Delworth, T. L.: Simulated response of the Pacific decadal oscillation to climate
805 change, Journal of Climate, 29(16), 5999-6018, <https://doi.org/10.1175/JCLI-D-15-0690.1>,
806 2016.

807 Zhang, R., and Delworth, T. L.: Impact of Atlantic multidecadal oscillations on India/Sahel rainfall and
808 Atlantic hurricanes, Geophysical research letters, 33(17),
809 <https://doi.org/10.1029/2006GL026267>, 2006.